

Article

MHD 3D Crossflow in the Streamwise Direction Induced by Nanofluid Using Koo–Kleinstreuer and Li (KLL) Correlation

Umair Khan ¹, Jamel Bouslimi ², Aurang Zaib ³, Fahad S. Al-Mubaddel ^{4,5}, Najma Imtiaz ⁶, Abdulaziz N. Alharbi ² and Mohamed R. Eid ^{7,8,*}

¹ Department of Mathematics and Social Sciences, Sukkur IBA University, Sukkur 65200, Pakistan; umairkhan@iba-suk.edu.pk

² Department of Physics, College of Science, Taif University, 11099, Taif 21944, Saudi Arabia; jamelabouiyes4@gmail.com (J.B.); alharbiaziz@tu.edu.sa (A.N.A.)

³ Department of Mathematical Sciences, Federal Urdu University of Arts, Science & Technology, Gulshan-e-Iqbal Karachi 75300, Pakistan; aurangzaib@fuuast.edu.pk

⁴ Department of Chemical Engineering, College of Engineering, King Saud University, P.O. Box 800, Riyadh 11421, Saudi Arabia; falmubaddel@ksu.edu.sa

⁵ Fellow, King Abdullah City for Renewable and Atomic Energy (KA-CARE) Energy Research and Innovation Center, (ERIC), Riyadh 11451, Saudi Arabia

⁶ Institute of Mathematics and Computer Science, University of Sindh, Jamshoro 76060, Pakistan; Najma.channa@usindh.edu.pk

⁷ Department of Mathematics, Faculty of Science, New Valley University, Al-Kharga, Al-Wadi Al-Gadid 72511, Egypt

⁸ Department of Mathematics, Faculty of Science, Northern Border University, Arar 1321, Saudi Arabia

* Correspondence: m_r_eid@yahoo.com



Citation: Khan, U.; Bouslimi, J.; Zaib, A.; Al-Mubaddel, F.S.; Imtiaz, N.; Alharbi, A.N.; Eid, M.R. MHD 3D Crossflow in the Streamwise Direction Induced by Nanofluid Using Koo–Kleinstreuer and Li (KLL) Correlation. *Coatings* **2021**, *11*, 1472. <https://doi.org/10.3390/coatings11121472>

Academic Editor: Eduardo Guzmán

Received: 5 October 2021

Accepted: 25 November 2021

Published: 30 November 2021

Publisher's Note: MDPI stays neutral with regard to jurisdictional claims in published maps and institutional affiliations.

Abstract: Aluminum nanoparticles are suitable for wiring power grids, such as local power distribution and overhead power transmission lines, because they exhibit high conductivity. These nanoparticles are also among the most utilized materials in electrical field applications. Thus, the present study investigated the impact of magnetic field on 3D crossflow in the streamwise direction with the impacts of Dufour and Soret. In addition, the effects of activation energy and chemical reaction were incorporated. The viscosity and thermal conductivity of nanofluids were premeditated by KKL correlation. Prominent PDEs (Partial Differential Equations) were converted into highly nonlinear ODEs (Ordinary Differential Equations) using the proper similarity technique and then analyzed numerically with the aid of the built-in bvp4c solver in MATLAB. The impact of diverse important variables on temperature and velocity was graphically examined. Additionally, the influences of pertaining parameters on the drag force coefficient, Nusselt number, and Sherwood number were investigated. Inspections revealed that the mass transfer rate decreases, while the heat transport increases with increasing values of the Soret factor. However, the Nusselt and Sherwood numbers validate the differing trend for rising quantities of the Dufour factor.

Keywords: double solutions; activation energy; crossflow; MHD (Magnetohydrodynamics); Soret and Dufour numbers; binary chemical reaction (BCR); nanofluid; KKL correlation



Copyright: © 2021 by the authors. Licensee MDPI, Basel, Switzerland. This article is an open access article distributed under the terms and conditions of the Creative Commons Attribution (CC BY) license (<https://creativecommons.org/licenses/by/4.0/>).

1. Introduction

Cross-boundary-layer flow (CBLF) is one of the most important BLs (Boundary-layers) in several engineering applications such as wind flow phenomena, aerospace, mechanical engineering, etc. Other examples of cross-boundary-layer flow include the flow of airplane swept-back wings, cones, spheres at an angle of attack, and spinning discs. It is critical to understand flow dynamics to determine how to sidestep the hazard of turbulence. Jones [1] revealed significant results for the problem of secondary flow by observing the key effect on the BL. He also discovered that as the coefficient of lift decreases, the stable area of laminar flow increases. Mager [2] inspected 3D flow through a flat surface, as well as a curved

surface, in a study that was heavily influenced by the element of the biggest principal case and moment velocity in the crosswise direction. Dwyer [3] investigated a crossflow problem containing 3D equations through the zero velocity of free-stream secondary flow and used the FDM (Finite Difference Method) to obtain a solution to 3D formulas. A closed-form solution of crosswise flow over a flat surface was reported by Loos [4], who deemed the parabolic shape of streamlines. Na and Hansen [5] addressed the steady flow of power-law index liquid under the presumption of crossflow. Two-dimensional (2D) flow and heat transmission with secondary flow over a cylinder were inspected by Karabulut and Ataer [6]. Fang and Lee [7] reported 3D flow in the spanwise crossflow direction with a moving boundary. The viscous dissipation effect on forced convective flow in the secondary or crossflow direction was examined by Bhattacharyya and Pop [8], who reported dual solutions for a moving constraint. Weidman [9] inspected crossflow through an exponentially stretchable power-law plate created by the speed of transverse wall shearing (WS). Weidman [10] observed the crossflow induced by the action of the transverse plate. Secondary flow in the streamwise direction via a moving sheet with convective constraints and viscous dissipation was presented by Haq et al. [11].

The study of the magnetic characteristics of electrically conducting fluids is known as magnetohydrodynamics (MHD). Magnetic fluids include plasmas, saltwater, electrolytes, and fluid metals. Research on magnetic fields is crucial in several engineering disciplines, including reactor cooling, power generation, crystal growth, fluid metal, magnetic drug targeting, etc. Alfven [12] began investigating magnetic fields. Ali et al. [13], Salem [14], Zaib et al. [15], and Azam et al. [16] investigated magnetic fluid flow via various aspects. Sheikholeslami [17] used Darcy's law to examine the impact of MHD on natural convection flow caused by a porous cavity. Additionally, the impact of heater-sink on magneto liquid flow in a square hollow by exploiting an artificial neural network with entropy generation was concluded by Rabbi et al. [18]. Recently, Ghadikolaei and Gholinia [19] investigated the effect of MHD on radiative 3D flow including hybrid nanomaterials caused by H_2 bonding of a vertical stretchable plate with suction and shape factors.

The concept of mass transfer occurs as a result of the well-known concentration disparity of species depicted in a concoction. It conveys them from a higher area of concentration to a lower area of concentration. There are many methods available in this splendid era, for example, absorption, thermal insulation, moisture/temperature dispersal from groove fields, distillation of alcohol, and processing of food via sufficient mass transport applications. Aside from that, mass transfer is important in most living matter procedures such as sweating, nutrition, and respiration. Abel et al. [20] explored the features of heat transfer, as well as mass transfer, by including hydromagnetic liquid motion from an extending plate induced by Walter's-B liquid. They considered two different cases of temperature at the boundary, namely prescribed wall heat flux (PHF) and prescribed surface temperature (PST). Kumar and Roy [21] scrutinized the impacts of heat and mass transfer on the mixed convective flow induced by unsteady rotating fluid past a vertical cone. Two different conditions were considered, namely PHF and PST. Chen [22] inspected the impact of viscous dissipation on MHD free convective flow via a vertical sheet with heat and mass transport. Because of the significance of incorporating mass transportation, Parmar et al. [23], Kandasamy et al. [24], Afify [25], and Rahman et al. [26] highlighted the aspect of this problem with dissimilar phenomena.

In mass transfer, there is a single significant condition that is not normally encountered in chemical species reactions via Arrhenius activation energy (AAE). Arrhenius coined the term "activation energy" in 1889. AAE is the minimum amount of energy required for a reagent to be converted into product form. The procedure of mass interaction in conjunction with BCR via AAE is traditionally important in oil reservoirs or geothermal engineering, a mechanism in liquid and oil dispersions, preparing food, and so on. Together with experimental efforts, theoretical results must be developed to evaluate the impact of AAE on fluid flow. Bestman [27] investigated the impact of activation energy on free convection flow from a moving permeable boundary wall in a porous medium. He

presented the results in the form of an asymptotic approximation for activation energy and larger suction. Mebine and Gumes [28] investigated the exothermic reaction and AAE on MHD flow through a special network. Khan et al. [29] studied the impacts of binary reaction and AAE on MHD cross liquid with mixed convective and nonlinear radiation. They inspected that species of concentration augments because of AAE and shrinks because of the Schmidt number. The impacts of BCR and AAE on 3D nonlinear radiative flow comprising non-Newtonian nanofluid over a slandering sheet with MHD and slip effects were inspected by Reddy et al. [30]. They discovered that activation energy and binary chemical parameters increase the mass transfer rate, while nanofluid temperature augments due to an erratic radiative parameter. Khan et al. [31] recently achieved multiple solutions of MHD crossflow concerning chemical reaction, activation energy, and nonlinear radiation induced by titanium alloy particles.

The combined effects of Soret and Dufour are crucially substantial for fluids with better concentration and temperature gradients, as well as in macroscopically essential physical phenomena in fluid mechanics. These effects are easily noted in areas of combustion flames, solar reactors, and collectors, along with the conservation of energy in some types of buildings. Mansour et al. [32] considered the effect of BCR on MHD free convective flow past a stretchable surface engrossed in a porous medium using the Soret and Dufour effects. Prasad et al. [33] investigated the effects of Soret and Dufour on MHD flow over a vertical sheet in a non-Darcian medium. Pal et al. [34] scrutinized the Soret and Dufour impacts on mixed convective flow past a nonlinear stretchable sheet induced via radiation effects. Zaib and Shafie [35] studied time-dependent flow past a stretchable sheet along with the viscous dissipation, Soret, radiation, and Dufour effects. The influences of Soret and Dufour on Lorentz forces flow conveying water-based Al_2O_3 and TiO_2 particles through a permeable stretchable sheet with absorption or generation of heat was examined by Reddy and Chamkha [36]. Khan et al. [37] presented the Soret and Dufour influences on Lorentz forces induced by non-Newtonian fluid past a stretchable cylinder with the Newtonian mass flux condition. They showed that the temperature and concentration fields enhanced because of thermal and solute factors. Recently, Idowu and Falodun [38] employed the technique of spectral relaxation to create a model involving non-Newtonian fluid past a semi-infinite plate with Dufour and Soret effects.

Examining the literature reveals that the model contains activation energy and binary reaction induced via aluminum nanofluid by utilizing KKL correlation through a crossflow not yet scrutinized. In addition, the base fluid in nanofluid may be considered Newtonian or non-Newtonian fluid. Devi and Devi [39], Soid et al. [40], and Aly and Pop [41] investigated nanofluid with Newtonian fluid as a base fluid. Islami et al. [42], Elgazery [43], and Hakeem et al. [44] considered non-Newtonian fluid as a base fluid to investigate nanofluid flow. In this paper, we investigate the effect of a binary chemical reaction and activation energy on a magnetic field induced by nanofluid with Newtonian fluid as a base fluid by employing KKL correlation via crossflow in the streamwise direction. In addition, the Dufour and Soret effects are incorporated. This evaluation provides a new method for scientists and researchers to learn about the properties of mass and heat transfer in the streamwise direction through crossflow. Experimental, as well as theoretical, efforts on improving heat transfer by the scattering of nanosolid particles in fluids have inspired researchers to develop numerous correlations for effective heat transfer (thermal properties, viscosity, thermal conductivity, etc.). The most recent model was presented by Koo, Kleinstreuer, and Liu (KKL). In recent years, scholars have investigated this model to demonstrate and explore numerous applications in technology and science. For example, Kandelousi [45] and Haq et al. [46] provided different applications by utilizing the KKL model in various geometries, whereas Alsagri and Moradi [47] introduced several applications to the KKL nanoliquid model. They addressed several other applications in nanofluid in problems of heat transfer between rotary tubes. Sheikholeslami and Mahian [48] investigated the improvement of PCM solidification, employing inorganic nanomaterials to display an application in energy storage using the KKL theory. The `bvp4c` solver is utilized to solve

the resultant model numerically. The effects of significant parameters are satisfied with the help of tables and graphs.

2. Mathematical Scenario of the Problem

The considered problem is formulated basically in the crossflow, secondary-flow, or streamwise direction comprising Al_2O_3 -water nanofluid using Koo–Kleinstreuer and Li (KKL) correlation within the boundary-layer technique. Following the phenomenon of secondary or cross flow, we investigated the impact of MHD 3D flow with binary chemical reaction and activation energy. The Soret and Dufour impacts are also discussed in the current research work. The geometrical framework of the flow and heat transfer problem in the presence of Al_2O_3 nanoparticles is confined with the help of a rectangular Cartesian coordinate system (x_h, y_h, z_h) , as shown in Figure 1, where the x_h (chordwise) coordinate is measured parallel to the surface of the flat plate, while the y_h coordinate is executed in the spanwise direction. Therefore, the assumed velocity (which is unchangeable) at the horizontal surface of the flat plate is mathematically denoted by $-U_d \varepsilon_d$, where ε_d is the dimensionless constant (the moving factor), and the exterior flow is signified by U_d (uniform velocity). The changeable magnetic field $B_h = B_0 / (2x_h)^{1/2}$ is exercised normal to the surface of the flat plate. The nanofluid is a mixture of two dissimilar components such as Al_2O_3 nanoparticles and H_2O (water) base fluids, while the properties of the considered nanofluid in the model are taken to be constant. The thermophysical properties of the nanofluid are given in Table 1. Additionally, the secondary flow has a broad range of levels and is supposed to be fully established in the spanwise direction. Hence, the succeeding basic steady governing equations can be read in the absence of the z_h coordinate. So, the equation of continuity for incompressible liquid is:

$$\frac{\partial u_h}{\partial x_h} + \frac{\partial v_h}{\partial y_h} = 0, \quad (1)$$

and the Navier–Stokes equations with a constant property are (see [8,11,49]):

$$u_h \frac{\partial u_h}{\partial x_h} + v_h \frac{\partial u_h}{\partial y_h} = -\frac{1}{\rho_{nf}} \frac{\partial p_h}{\partial x_h} + \nu_{nf} \left(\frac{\partial^2 u_h}{\partial y_h^2} \right) - \frac{\sigma_{nf} B_h^2}{\rho_{nf}} u_h, \quad (2)$$

$$u_h \frac{\partial v_h}{\partial x_h} + v_h \frac{\partial v_h}{\partial y_h} = -\frac{1}{\rho_{nf}} \frac{\partial p_h}{\partial y_h} + \nu_{nf} \left(\frac{\partial^2 v_h}{\partial y_h^2} \right), \quad (3)$$

$$u_h \frac{\partial w_h}{\partial x_h} + v_h \frac{\partial w_h}{\partial y_h} = -\frac{1}{\rho_{nf}} \frac{\partial p_h}{\partial z_h} + \nu_{nf} \left(\frac{\partial^2 w_h}{\partial y_h^2} \right) - \frac{\sigma_{nf} B_h^2}{\rho_{nf}} w_h, \quad (4)$$

Now, exercising the boundary-layer approximation or scaling transformation, Equation (3) of the y -momentum completely disappears, while by the Bernoulli equation, Equations (2) and (4) reduce to the following simplified form as follows:

$$-\frac{1}{\rho_{nf}} \frac{\partial p_h}{\partial x_h} = \frac{\sigma_{nf} B_h^2}{\rho_{nf}} U_d, \quad (5)$$

$$-\frac{1}{\rho_{nf}} \frac{\partial p_h}{\partial z_h} = \frac{\sigma_{nf} B_h^2}{\rho_{nf}} W_d, \quad (6)$$

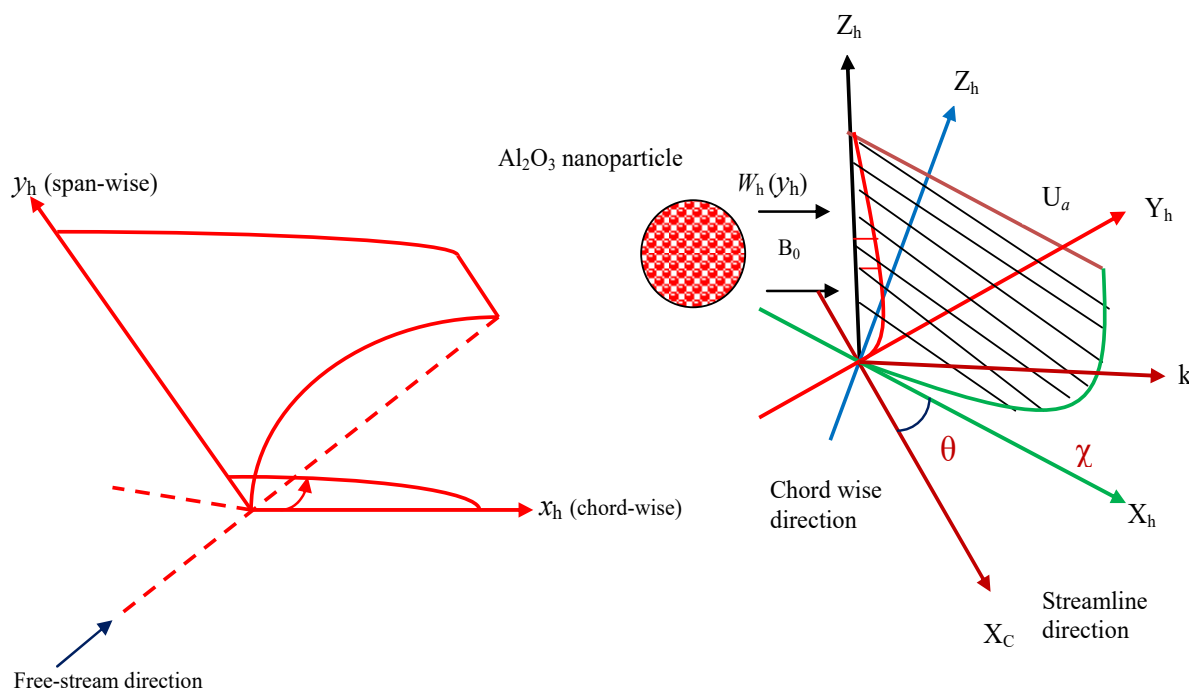


Figure 1. Physical illustration of the problem.

Eliminating the pressure term from Equations (2) and (4), one obtains:

$$u_h \frac{\partial u_h}{\partial x_h} + v_h \frac{\partial u_h}{\partial y_h} = \nu_{nf} \left(\frac{\partial^2 u_h}{\partial y_h^2} \right) + \frac{\sigma_{nf} B_h^2}{\rho_{nf}} (U_d - u_h), \tag{7}$$

$$u_h \frac{\partial w_h}{\partial x_h} + v_h \frac{\partial w_h}{\partial y_h} = \nu_{nf} \left(\frac{\partial^2 w_h}{\partial y_h^2} \right) + \frac{\sigma_{nf} B_h^2}{\rho_{nf}} (W_d - w_h), \tag{8}$$

In addition, the temperature T_h and concentration C_h are presumed to be constants at the surface, whereas the free-stream temperature and free-stream concentration are T_∞, C_∞ , respectively. Therefore, the temperature and concentration equations are:

$$u_h \frac{\partial T_h}{\partial x_h} + v_h \frac{\partial T_h}{\partial y_h} = \frac{k_{nf}}{(\rho c_p)_{nf}} \frac{\partial^2 T_h}{\partial y_h^2} + \frac{D_m k_T}{c_s c_p} \frac{\partial^2 C_h}{\partial y_h^2}, \tag{9}$$

$$u_h \frac{\partial C_h}{\partial x_h} + v_h \frac{\partial C_h}{\partial y_h} = D_B \frac{\partial^2 C_h}{\partial y_h^2} - k_{rd}^2 \left(\frac{T_h}{T_\infty} \right)^m e^{-\frac{E_d}{\kappa_d T_h}} (C_h - C_\infty) + \frac{D_m k_T}{T_m} \frac{\partial^2 T_h}{\partial y_h^2}, \tag{10}$$

and the boundary conditions (BCs) are:

$$\begin{aligned} u_h &= -U_d \varepsilon_d, w_h = 0, v_h = v_d, T_h = T_w, C_h = C_w \text{ at } y_h = 0, \\ u_h &\rightarrow U_d, w_h \rightarrow W_d, T_h \rightarrow T_\infty, C \rightarrow C_\infty \text{ as } y_h \rightarrow \infty. \end{aligned} \tag{11}$$

Now, in the above governing equations, the velocity components are (u_h, v_h, w_h) in the requisite rectangular Cartesian coordinates (x_h, y_h, z_h) , respectively, and p_h is the pressure of the fluid. In Equation (10), the second term on the right-hand side of the equation is the Arrhenius function $k_{rd}^2 (T_h/T_\infty)^m \exp(-E_d/\kappa_d T_h)$, with a particular value of the Boltzmann constant $\kappa_d = 8.61 \times 10^{-5}$ eV/K; m is the rate of fitted constant, which is bounded in the range of $(-1, 1)$; and k_{rd} is the chemical reaction rate. Additionally, the other constraints used in the governing equations are D_m, c_s, k_T, c_p , and T_m : the coefficient of mass diffusivity, concentration of susceptibility, thermal diffusion ratio, specific heat at constant pressure, and mean fluid temperature, respectively.

Moreover, the other coefficients or symbols contained in the governing equations for the nanofluid are the specific heat capacitance at constant pressure $(\rho c_p)_{nf}$, density ρ_{nf} , and electrical conductivity σ_{nf} . The expression for these physical properties of the nanofluid is given by ([50,51]):

$$\begin{aligned} \rho_{nf} &= \phi \rho_s + (1 - \phi) \rho_f, (\rho c_p)_{nf} = \phi (\rho c_p)_s + (1 - \phi) (\rho c_p)_f, \\ \sigma_{nf} &= \left[1 + \frac{3(\sigma_s/\sigma_f - 1)\phi}{(\sigma_s/\sigma_f + 2) - (\sigma_s/\sigma_f - 1)\phi} \right] \sigma_f. \end{aligned} \quad (12)$$

Therefore, ρ_f , σ_f , and $(\rho c_p)_f$ are the specific heat capacity, density, and electrical conductivity of the base fluid, respectively, while the same quantities are used for the nanoparticles whose subscript includes the letter s . Additionally, ϕ is the nanoparticles' volume fraction.

The Brownian motion fundamentally affects the current k_{nf} thermal conductivity (TCN). Koo and Kleinstreuer [52] recommended that k_{nf} be made from the particle's conservative stationary part and a posited Brownian motion (BMN) quantity. This mutual TCN model considers the impacts of particle volume fraction, particle size, and dependency just as kinds of particle and base liquefied balances

$$k_{nf} = k_{\text{Brownian}} + k_{\text{static}}, \quad (13)$$

$$\frac{k_{\text{static}}}{k_f} = 1 + \frac{3\left(\frac{k_s}{k_f} - 1\right)\phi}{\left(\frac{k_s}{k_f} + 2\right) - \left(\frac{k_s}{k_f} - 1\right)\phi}, \quad (14)$$

where k_{static} represents static TCN dependent on Maxwell's usual correlation. The upgraded TCN part produced by the small convective heat transfer rate of a particle's BMN and influenced by a free-stream fluidic motion is acquired by reproducing Stokes' flow near a sphere of influence (nanoparticle). By presenting two experimental constraints (γ and h), Koo [53] consolidated the collaboration between nanomaterials in correlation with the temperature impact in the given model, regarded as:

$$k_{\text{Brownian}} = 5 \times 10^4 \gamma \phi \rho_f c_{s,f} \sqrt{\frac{\kappa_s T_h}{\rho_s d_s}} h(T_h, \phi). \quad (15)$$

Lately, there has been an expanding pattern to stress the significance of the interfacial heat obstruction among nanomaterials and based liquids (see Jang and Choi [54] and Prasher et al. [55]). The heat interfacial opposition (Kapitza obstruction) is accepted to exist in the nearby layers of the two distinct constituents. The thin barrier layer assumes an important part in debilitating the viable TCN of the nanoparticle.

Li [56] returned to the model introduced by Koo and Kleinstreuer [52] and joined γ and h functions to introduce another H function that catches the impacts of particle width, volume fraction rate, and temperature. The experimental H -function relies on the kind of nanoliquid [56]. Additionally, by making known a thermal interfacial resistance (TIR) $R_f = 4 \times 10^{-8} \text{ km}^3/\text{W}$, the unique k_s in Equation (15) above is substituted by a novel $k_{s,eff}$ in the system:

$$R_f + \frac{d_s}{k_s} = \frac{d_s}{k_{s,eff}}. \quad (16)$$

For liquids of different bases and diverse nanomaterials, the function ought to appear as something else. Just water-based nanofluid is deliberated in the present study. For Al_2O_3 -water nanofluid, this function adopts the pattern:

$$H(T_h, \phi, d_s) = \left(c_1 + c_2 \ln(d_s) + c_5 \ln(d_s)^2 + c_3 \ln(\phi) + c_4 \ln(d_s) \ln(\phi) \right) \ln(T_h) + \left(c_6 + c_7 \ln(d_s) + c_{10} \ln(d_s)^2 + c_8 \ln(\phi) + c_9 \ln(d_s) \ln(\phi) \right) \quad (17)$$

$$\phi \leq 0.04, \quad 300\text{K} \leq T_b \leq 325\text{K}$$

Using the coefficients, c_j ($j = 1 \dots 10$) is built on the nature of nanomaterials, and also, with the occurrences of these arbitrary constant coefficients, Al_2O_3 -water nanofluid has an R^2 of 96% and 98%, correspondingly [50] (Table 2). To conclude, the KKL correlation is pointed out as:

$$k_{\text{Brownian}} = 5 \times 10^4 \phi \rho_f c_{s,f} \sqrt{\frac{\kappa_s T_h}{\rho_s d_s}} H(T_h, \phi, d_s). \quad (18)$$

Koo and Kleinstreuer [52] additionally took into consideration the laminar type of induced nanofluid flow in a micro heat-sink through the powerful nanofluid TCNM that they recognized (KKL [52]). For the powerful viscosity owing to micromixing in suspensions, they deliberate:

$$\mu_{nf} = \mu_{\text{Brownian}} + \mu_{\text{static}} = \mu_{\text{static}} + \frac{\mu_f k_{\text{Brownian}}}{\text{Pr} k_f}, \quad (19)$$

where $\mu_{\text{static}} = \frac{\mu_f}{(1-\phi)^{2.5}}$, shows the nanofluid's viscosity, which is specified as formerly by Brinkman. The following self-similarity variables are given by [52]:

$$\xi = y_h \sqrt{\frac{U_d}{2x_h v_f}}, \quad \psi_d = \sqrt{2x_h U_d v_f} F(\xi), \quad w_h = W_d G(\xi), \quad (20)$$

$$\theta(\xi) = \frac{T_\infty - T_h}{T_\infty - T_w}, \quad S(\xi) = \frac{C_\infty - C_h}{C_\infty - C_w}$$

Here, in Equation (20), the posited stream function designated by ψ_d and v_f is the kinematic viscosity. The above transformations substituted in the governing Equations (7)–(10), along with the BCs (11), result in the reduced form of the ODEs:

$$\frac{\mu_{nf}}{\mu_f} F''' + \frac{\rho_{nf}}{\rho_f} F F'' + M \frac{\sigma_{nf}}{\sigma_f} (1 - F') = 0, \quad (21)$$

$$\frac{\mu_{nf}}{\mu_f} G'' + \frac{\rho_{nf}}{\rho_f} F G' + M \frac{\sigma_{nf}}{\sigma_f} (1 - G) = 0, \quad (22)$$

$$\frac{k_{nf}}{k_f} \theta'' + \text{Pr} \frac{(\rho c_p)_{nf}}{(\rho c_p)_f} (F \theta' + D u_d S'') = 0 \quad (23)$$

$$S'' + Le_d F S' - \beta_d Le_d (1 + \delta_d \theta)^m \exp \left[\frac{-e_d}{1 + \delta_d \theta} \right] S + Sr_d Le_d \theta'' = 0 \quad (24)$$

The subjected major boundary restrictions are:

$$\left. \begin{aligned} F'(0) = \varepsilon_d, \quad F(0) = f_w, \quad G(0) = 0, \quad \theta(0) = 1, \quad S(0) = 1, \\ F'(\infty) \rightarrow 1, \quad G(\infty) \rightarrow 1, \quad \theta(\infty) \rightarrow 0, \quad S(\infty) \rightarrow 0. \end{aligned} \right\} \quad (25)$$

The following distinguished constraints occurred in the above similarity equations, which are mathematically expressed as:

$$M_d = \frac{\sigma_f B_0^2}{\rho_f U_d}, \text{Re}_{x_h} = \frac{x_h U_d}{\nu_f}, \text{Pr} = \frac{\nu_f}{\alpha_f}, e_d = \frac{E_d}{k_f T_\infty}, Sr_d = \frac{D_m k_T (T_w - T_\infty)}{\nu_f T_m (C_w - C_\infty)},$$

$$\beta_d = 2 \frac{\text{Re}_{x_h} \nu_f k_r d^2}{U_d^2}, \delta_d = \frac{T_w - T_\infty}{T_\infty}, Du_d = \frac{D_m k_T (C_w - C_\infty)}{\nu_f c_p (T_w - T_\infty)}.$$

These factors are namely demarcated as magnetic parameter M_d , Prandtl number Pr , activation parameter e_d , Reynolds number Re_{x_h} , reaction rate β_d , temperature difference parameter δ_d , Soret number Sr_d , and Dufour number Du_d .

Table 1. Thermophysical properties of the nanofluid [36].

Physical Properties	Water	Al ₂ O ₃
k (W/mK)	0.613	25
c_p (J/kg K)	4179	765
ρ (kg/m ³)	997.1	3970
σ (Ωm) ⁻¹	0.05	1×10^{-10}
d_s (nm)	-	47
Pr	6.2	-

Table 2. Constants of Al₂O₃-water.

Coefficient Values	Al ₂ O ₃ -Water
c_1	52.813
c_2	6.115
c_3	0.695
c_4	4.1×10^{-2}
c_5	0.176
c_6	-298.198
c_7	-34.532
c_8	-3.922
c_9	-0.235
c_{10}	-0.999

2.1. Skin Friction

The skin friction coefficients or friction factors in the streamwise and crossflow directions are defined as follows [49]:

$$C_{Fx_h} = \frac{\mu_{nf} \left(\frac{\partial u_h}{\partial y_h} \right)_{y_h=0}}{\rho_f U_d} = \frac{\mu_{nf}}{\mu_f} \frac{F''(0)}{\sqrt{2\text{Re}_{x_h}}} \tag{26}$$

$$C_{Gz_h} = \frac{\mu_{nf} \left(\frac{\partial w_h}{\partial y_h} \right)_{y_h=0}}{\rho_f W_d^2} = \frac{\mu_{nf}}{\mu_f} \frac{G'(0)}{\sqrt{2\text{Re}_{x_h}} (W_d/U_d)} \tag{27}$$

2.2. Nusselt Number

The heat transfer rate is defined as:

$$Nu_{x_h} = \frac{x_h \left(-k_{nf} \frac{\partial T_h}{\partial y_h} \right)_{y_h=0}}{k_f (T_w - T_\infty)} = - \frac{k_{nf}}{k_f} \frac{\theta'(0)}{\sqrt{2\text{Re}_{x_h}}} \tag{28}$$

2.3. Sherwood Number

The mass transfer rate is defined as:

$$Sh_{x_h} = \frac{x_h \left(-D_B \frac{\partial C_h}{\partial y_h} \right)_{y_h=0}}{D_B (C_w - C_\infty)} = -\frac{S'(0)}{\sqrt{2Re_{x_h}}} \quad (29)$$

where $Re_{x_h} = x_h U_d / \nu_f$ is the Reynolds number.

3. Methodology of the Considered Approach

The system of the nonlinear ODEs is calculated using the built-in MATLAB function `bvp4c`, i.e., boundary value problem of the fourth-order. This method is based on finite-difference code that utilizes the three-stage Lobatto IIIA formula. This formula, commonly known as the collocation formula, yields a C_1 continuous solution with fourth-order precision in the closed bounded interval from a to b . The best selection choice of the mesh point, along with the error control, is achieved by exercising the residual of the continuous outcome. In the MATLAB code, we utilized the syntax, which is followed as

$$\text{Sol} = (\text{bvp4c} (@\text{odefun}, @\text{bcfun}, \text{solinit}, \text{options}))$$

The set of nonlinear ODEs (21)–(24), along with BCs (25), are transmuted to the subsequent system of first-order ODEs to use this approach. To continue our working procedure, here, we allow new variables such as F by C_1 , G by C_4 , θ by C_6 , and S by C_8 for changing the boundary-values problem (BVP) into the initial-value problem (IVP):

$$C_1' = C_2, \quad C_2' = C_3, \quad (30)$$

$$C_3' = \frac{1}{\frac{\mu_{nf}}{\mu_f}} \left(-\frac{\rho_{nf}}{\rho_f} C_1 C_3 - M_d \frac{\sigma_{nf}}{\sigma_f} (1 - C_2) \right), \quad (31)$$

$$C_4' = C_5, \quad (32)$$

$$C_5' = \frac{1}{\frac{\mu_{nf}}{\mu_f}} \left(-\frac{\rho_{nf}}{\rho_f} C_1 C_5 - M_d \frac{\sigma_{nf}}{\sigma_f} (1 - C_4) \right), \quad (33)$$

$$C_6' = C_7, \quad (34)$$

$$C_7' = -\text{Pr} \frac{\frac{(\rho c_p)_{nf}}{(\rho c_p)_f}}{\frac{k_{nf}}{k_f}} (C_1 C_7 + D u_d C_9'), \quad (35)$$

$$C_8' = C_9, \quad (36)$$

$$C_9' = -Le_d C_1 C_9 + \beta_d Le_d (1 + \delta_d C_6)^m \exp \left[-\frac{e_d}{1 + \delta_d C_6} \right] C_8 - Sr_d Le_d C_7', \quad (37)$$

and the subject ICs are:

$$\left. \begin{aligned} C_2(0) = \varepsilon_d, \quad C_1(0) = f_w, \quad C_4(0) = 0, \quad C_7(0) = 1, \quad C_9(0) = 1, \\ C_2(\infty) \rightarrow 1, \quad C_4(\infty) \rightarrow 1, \quad C_7(\infty) \rightarrow 0, \quad C_9(\infty) \rightarrow 0. \end{aligned} \right\} \quad (38)$$

To meet the convergence conditions, a tolerance of 10^{-6} is considered during the calculations. It is worth noting that the two distinct solution branches are obtained by using different estimate values for the actual numbers. The procedure can be seen through the flow chart in Figure 2.

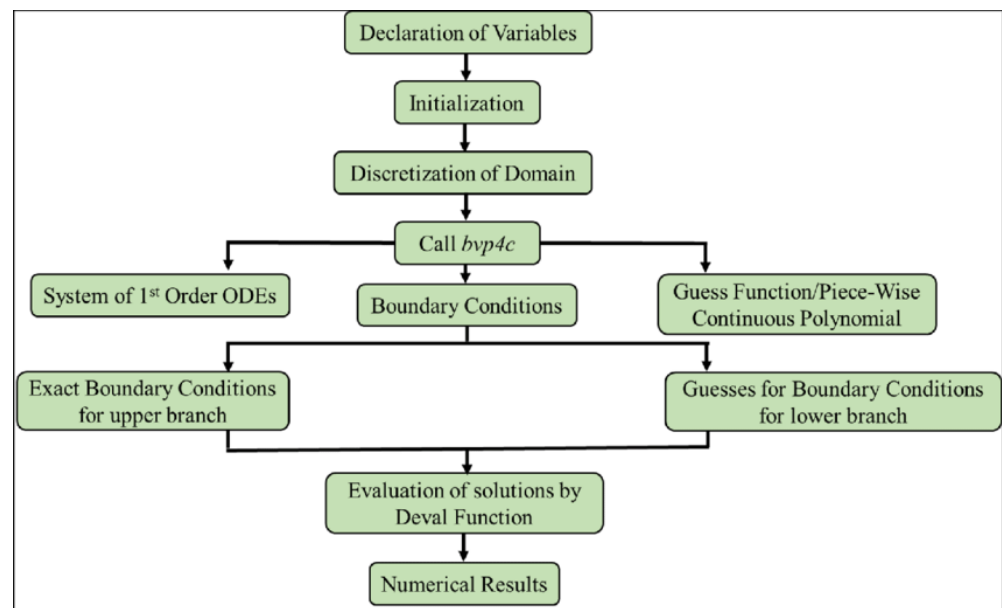


Figure 2. Flow chart to describe the numerical technique.

4. Results and Discussion

The similarity equations of the momentum, energy, and concentration are physically scrutinized in the current section of the research work using Koo–Kleinstreuer and Li (KKL) correlation to investigate the impacts of activation energy, Dufour numbers, binary chemical reaction, MHD, and Soret numbers over the streamwise and secondary-flow directions for the upper and lower solution branches comprising nanofluid (Al_2O_3 -water). In addition, the distinguished parameters, which are available in the model, are the following: $M_d, \phi, f_w, m, \varepsilon_d, Du_d, Le_d, e_d, \delta_d, Sr_d, \beta_d$, and Pr. Furthermore, the simulations of the entire paper were completed with the corresponding fixed values of these parameters, which can be read as 0.1, 0.025, 1, 0.4, 0.3, 0.5, 0.5, . . . , and 6.2, respectively. The comparison and outcomes of the considered model in terms of the upper and lower solution branches are graphically shown in Figures 3–22. These graphs depict the two distinct branch solutions for the various involved controlling parameters, which are bound in the form of velocity profile (x_h - and z_h -directions), temperature, concentration, friction factor, heat, and mass transfer fluxes. The solutions of the upper and lower branches are indicated by black solid and dashed lines, respectively. So, the point where these solutions meet is called the bifurcation or critical point, and it is represented by a small solid ball, as shown in each window of the engineering quantities of interest. Moreover, the given scheme and the simulations of the code were authenticated graphically for the dual-nature outcomes of Bhattacharyya and Pop [8], as shown in Figure 3, for secondary flow across a moving surface with limited situations. The evaluations demonstrate a high level of settlement between the published and current accessible findings.

Figures 4–7 exemplify the impacts of f_w on friction factors in the x_h - and z_h -axes directions, heat transfer, and mass transfer of the Al_2O_3 -water nanofluid versus ε_d for the solution of the upper and lower branch, respectively. From these figures, it is observed that the critical or bifurcation values $\varepsilon_d = \varepsilon_{d\text{Critical}}$ upsurge due to the larger values of f_w . Meanwhile, the bifurcation values are mathematically signified as ($\varepsilon_{d\text{Critical}} = 0.5917, 1.0908, 1.6240$). As a result, f_w postpones the separation of the boundary layer. The friction factors in the x_h - and z_h -axes directions increase in the upper branch solution due to the continuous increment in the values of the f_w , while they are reduced in the branch of lower solutions. From a physical point of view or scenario, a lot of liquid is pulled into the surface, and the liquid becomes more difficult to move, due to which the shear stress grows on the surface. In addition, the negative values of the shear stress in Figures 4 and 5 display that the surface exerts a drag force on the liquid, whereas the positive values show the opposite tendency. On the other hand, the

rate of heat transfer is significantly weakened in both solution branches (upper and lower) due to the escalation in the values of f_w as shown in Figure 6, while the mass transfer rate shows rising patterns in the branch of the upper and lower solutions, as shown in Figure 7. So, if the suction parameter influences the upsurge, the domain of the solution shrinks for the heat transfers and rises for the mass transfer. It appears that the solutions in the case of shrinking flow do not survive because the vorticity may not be confined within a boundary layer. However, the outcomes may occur if there is an accumulation of the impact of the mass suction parameter at the edge of the boundary layer to hold the vorticity. Additionally, in the case of shrinking velocity, the local mass transfer rate, as well as the local heat transfer rate, is higher than in the case of stretching velocity.

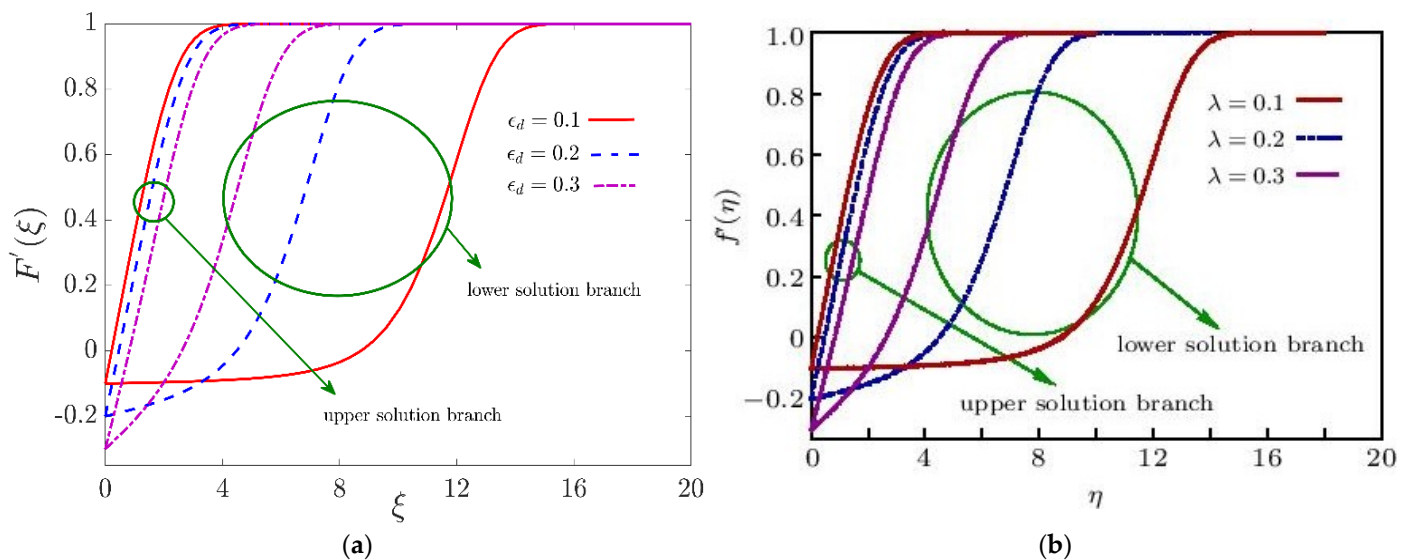


Figure 3. Graphical comparison of the velocity field (a) $F'(\xi)$ for ϵ_d with (b) Bhattacharyya and Pop [8].

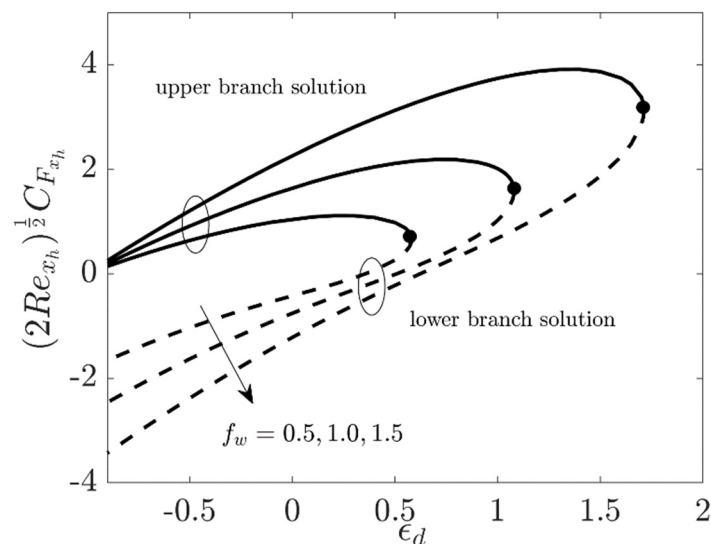


Figure 4. Impact of f_w on $(2Re_{x_h})^{1/2} C_{F_{x_h}}$.

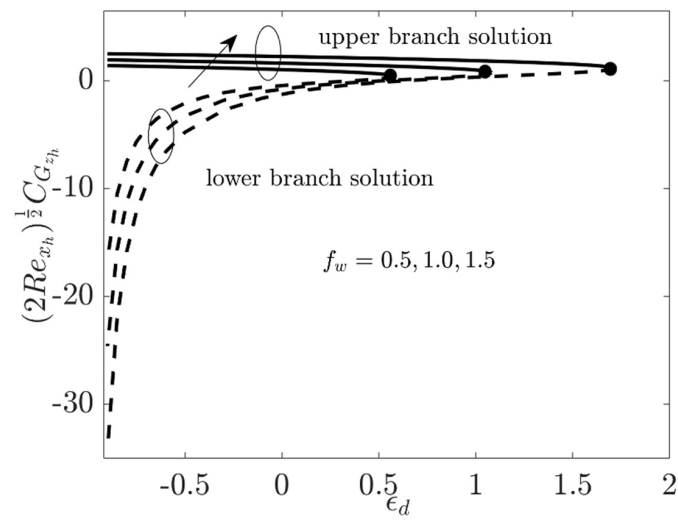


Figure 5. Impact of f_w on $(2Re_{x_h})^{1/2} C_{G_{x_h}}$.

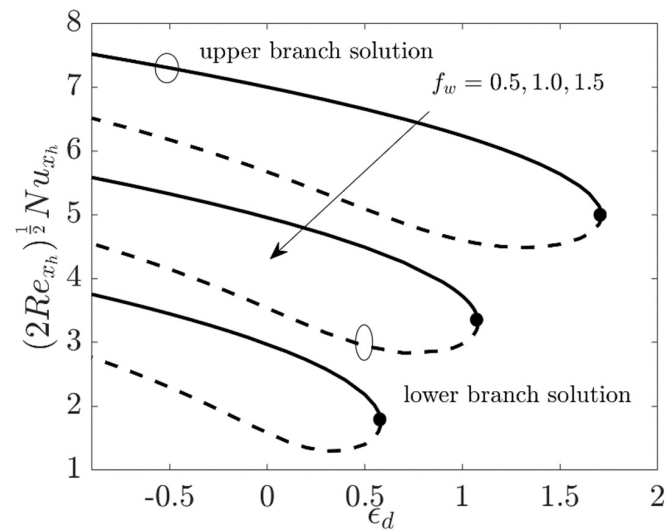


Figure 6. Impact of f_w on $(2Re_{x_h})^{1/2} Nu_{x_h}$.

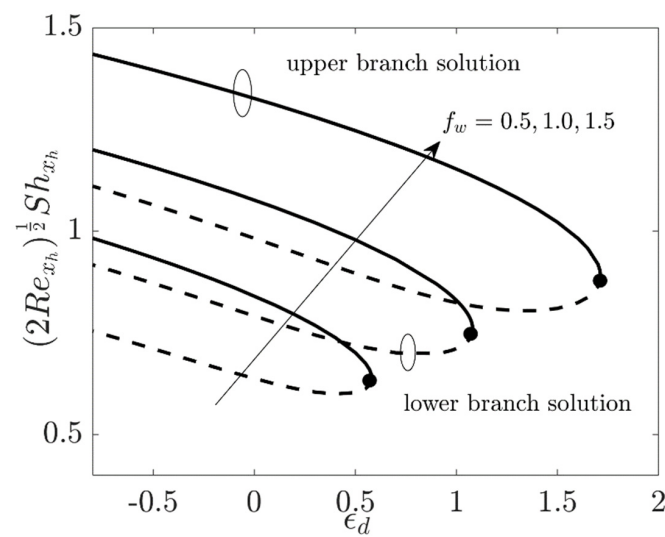


Figure 7. Impact of f_w on $(2Re_{x_h})^{1/2} Sh_{x_h}$.

The impacts of e_d and δ_d on the mass transfer rate for the two distinct solution branches against the moving parameter ϵ_d of the Al_2O_3 -water nanofluid are explicitly shown in Figures 8 and 9, respectively. The outcomes certify that the values of the mass transfer rate grow higher and higher in the branch of the upper solution, as well as in the lower solution, due to the larger values of the parameters e_d and δ_d . Moreover, the thickness of the concentration boundary layer is higher with larger values of ϵ_d and δ_d . The gap in the lower solution branch is slightly higher compared to the upper solution branch.

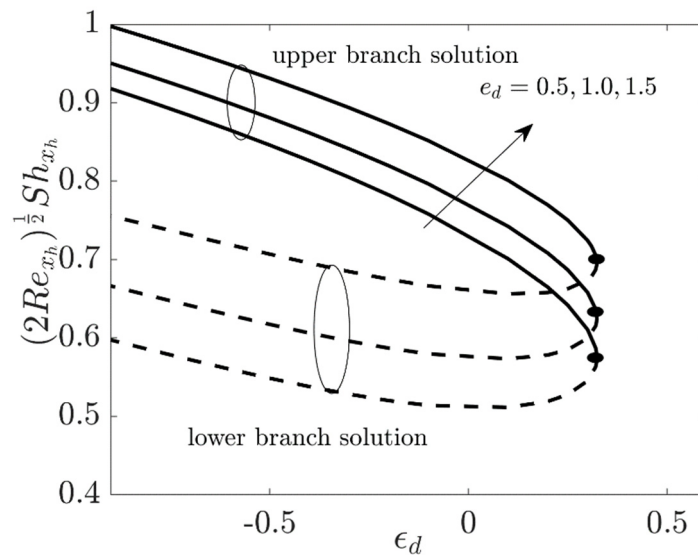


Figure 8. Impact of e_d on $(2Re_{x_h})^{1/2}Sh_{x_h}$.

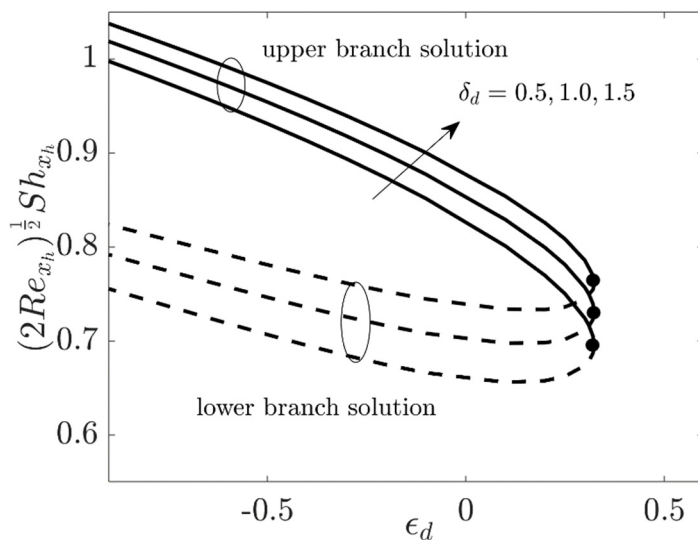


Figure 9. Impact of δ_d on $(2Re_{x_h})^{1/2}Sh_{x_h}$.

Figures 10 and 11 describe the variations in the heat and mass transfer fluxes for the two distinct branch solutions of the Al_2O_3 -water nanofluid against ϵ_d due to the influence of the parameter Du_d , respectively. The values of the heat transfer rate shrink in both solution branches (upper and lower) due to the augmentation in the values of Du_d , while the behavior of the solutions completely reverses for the mass transfer rate in both solution branches. In addition, the thermal boundary-layer thickness is reduced with higher Du_d , while on the other hand, the concentration boundary-layer thickness is improved.

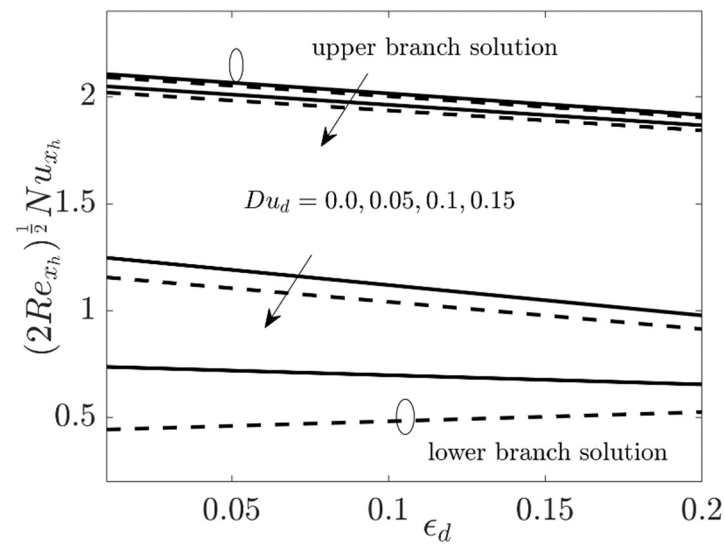


Figure 10. Impact of Du_d on $(2Re_{x_h})^{1/2} Nu_{x_h}$.

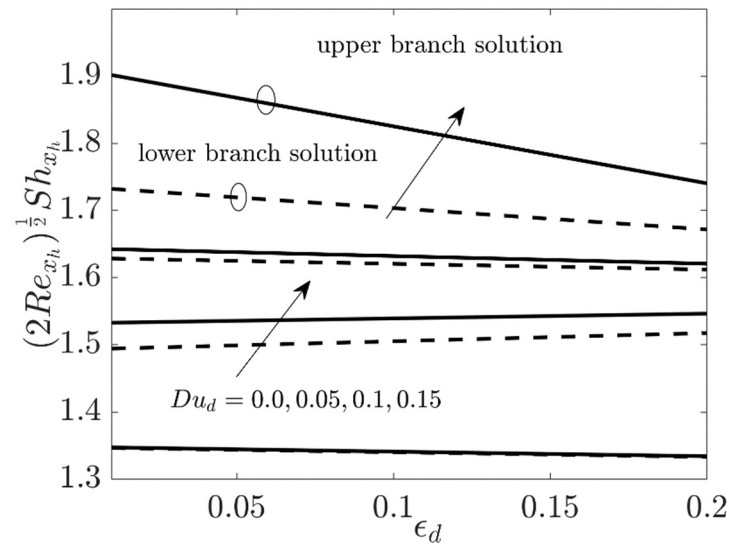


Figure 11. Impact of Du_d on $(2Re_{x_h})^{1/2} Sh_{x_h}$.

The influences of the Soret number Sr_d on the heat and mass transfer fluxes for the solution of the upper branch, as well as the lower branch, of the Al_2O_3 -water nanofluid versus the moving parameter ϵ_d are illustrated in Figures 12 and 13, respectively. These outcomes are in line with the solutions of Dzulkipli et al. [57]. From these figures, we see that the heat transfer rate continuously upsurges in both solution branches, while the mass transfer rate reduces in the upper and lower branches if we increase Sr_d . In addition, the thickness of the concentration boundary layer is higher with larger values of Sr_d .

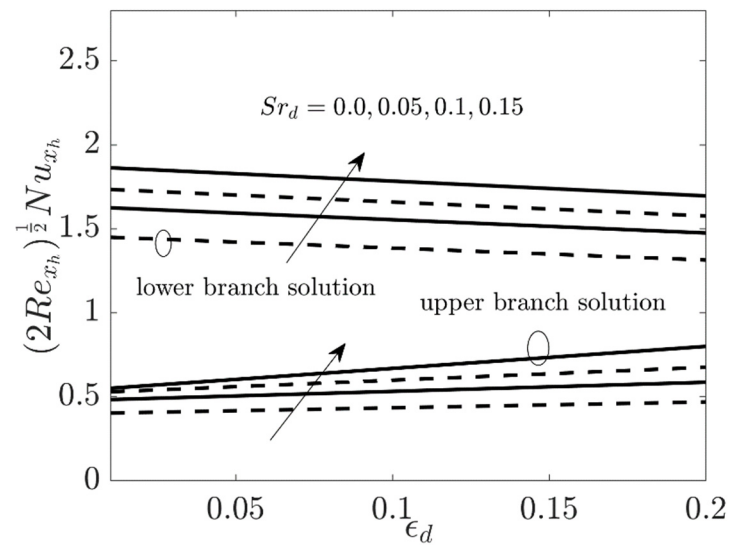


Figure 12. Impact of Sr_d on $(2Re_{x_h})^{1/2} Nu_{x_h}$.

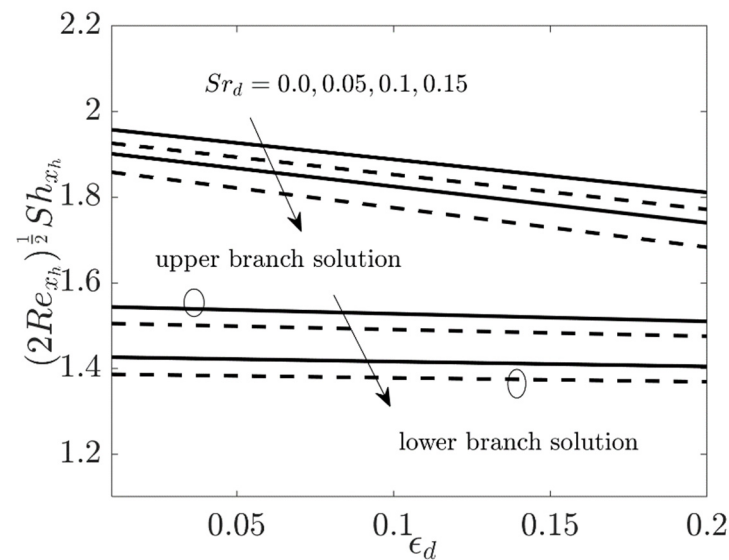


Figure 13. Impact of Sr_d on $(2Re_{x_h})^{1/2} Sh_{x_h}$.

The velocity profile in both directions (x_h - and z_h -axes) for the upper and lower solution branches of the Al_2O_3 -water nanofluid against the pseudosimilarity variable ζ due to the larger values of f_w is represented in Figures 14 and 15, respectively. From the results, it is seen that the velocities in both directions (x_h - and z_h -axes) for the upper branch solution increase due to the larger factor values of f_w , lowering the corresponding boundary-layer thicknesses, but the lower branch solution velocities decline. This is because when f_w increases, the velocity dispersion into the liquid becomes shorter.

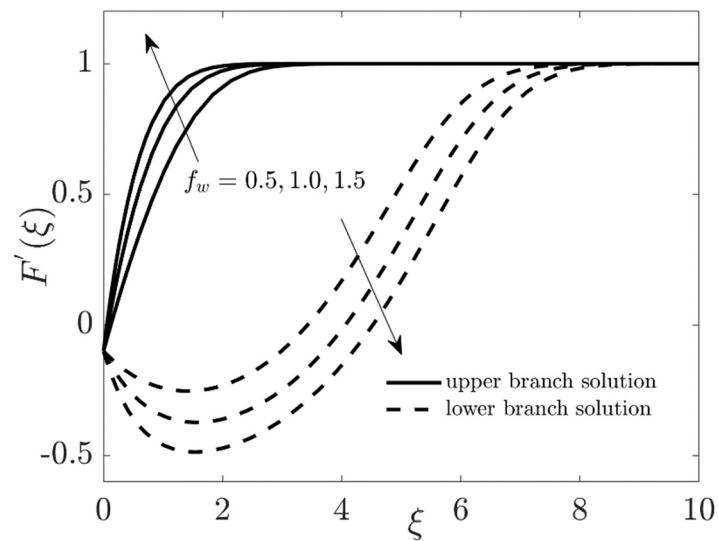


Figure 14. Impact of f_w on $F'(\xi)$.

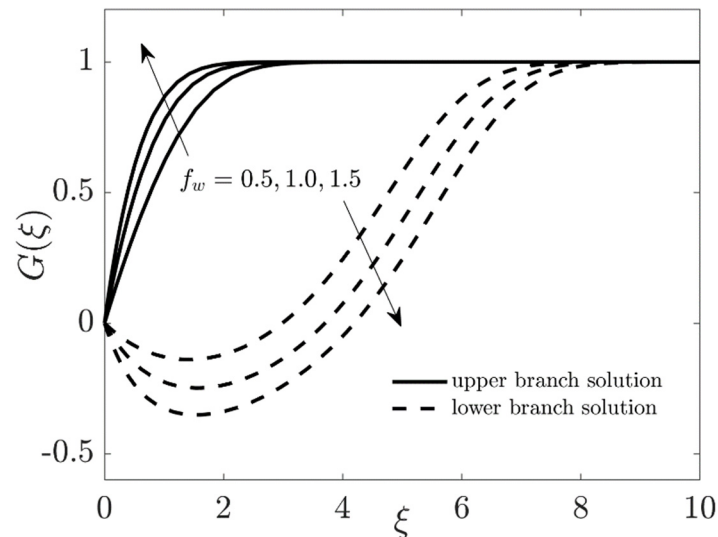


Figure 15. Impact of f_w on $G(\xi)$.

The impact of f_w on the temperature distribution and concentration profile of the Al_2O_3 -water nanofluid for the upper and lower solution branches is graphically highlighted in Figures 16 and 17, respectively. The temperature distributions and concentration profiles of the Al_2O_3 -water nanofluid in both solution branches are significantly declined due to the augmentation in the values of f_w . Moreover, the thermal and concentration boundary-layer thickness decline when increasing the values of f_w . In general, the explanation for this phenomenon is that the liquid is brought closer to the surface, causing the thickness of the thermal boundary layer to decrease. As a result, additional temperature is formed, which raises the fluid temperature.

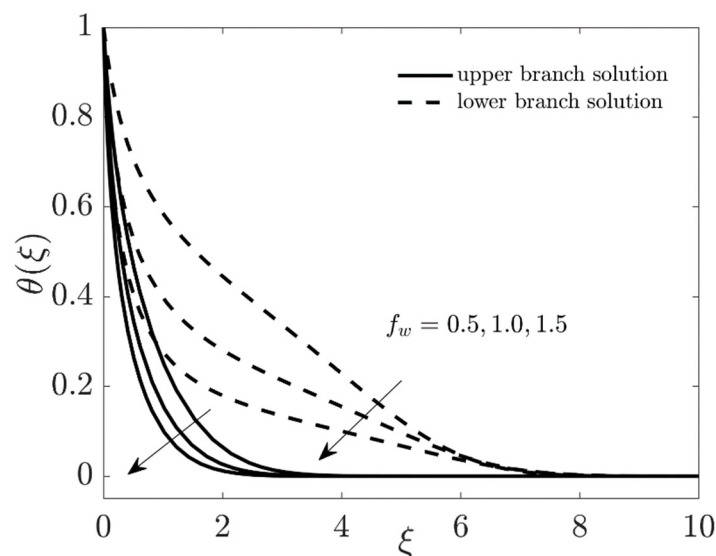


Figure 16. Impact of f_w on $\theta(\xi)$.

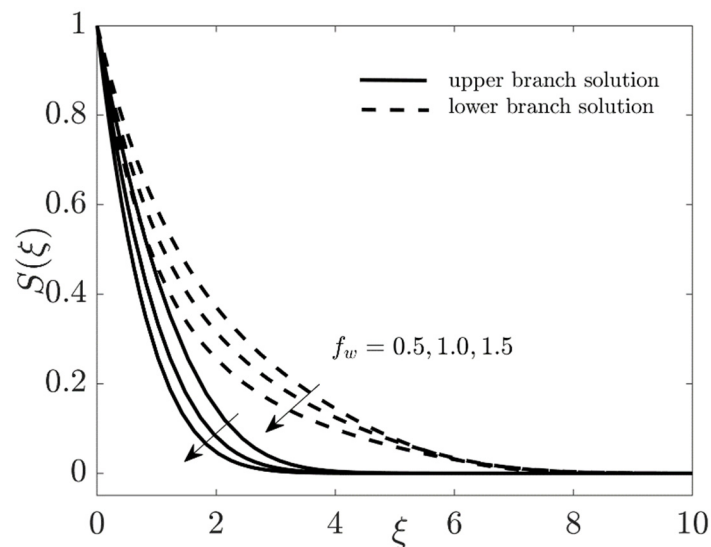


Figure 17. Impact of f_w on $S(\xi)$.

Figures 18 and 19 display the impact of ϕ on the velocity profile in both the x_h - and z_h -axes directions for the upper and lower solution branches, respectively. From both pictures, it is noted that the profile of velocity in both the x_h - and z_h -axes directions are decreased in the upper branch solution and increased in the lower branch solution due to the larger value of ϕ . The momentum boundary-layer thickness is diminished due to the augmentation in the value of ϕ . Moreover, the temperature and concentration profiles with the reassurance of ϕ for the two distinct branch solutions are captured in Figures 20 and 21, respectively. For growing values of ϕ , the temperature profile is enhanced in both branches of the outcomes, while the behavior of the solution is opposite for the concentration profile. Generally, the nanoparticle influences increase the thermal conductivity of the fluid. As a consequence, the temperature and the thermal boundary-layer thickness are boosted.

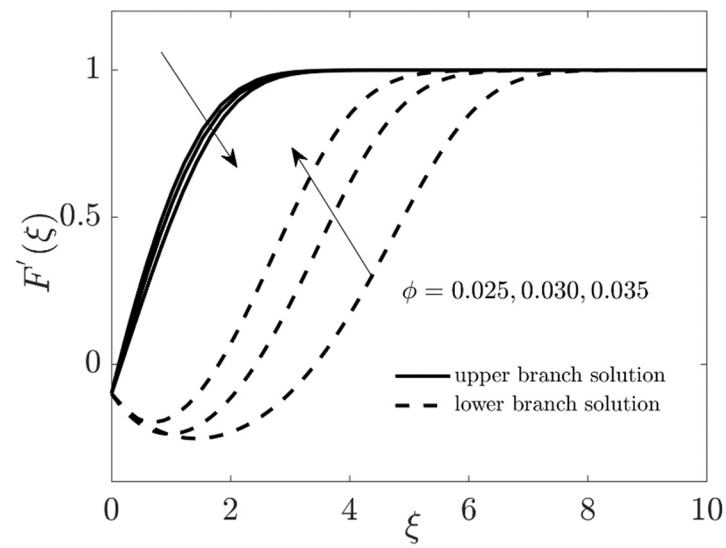


Figure 18. Impact of ϕ on $F'(\xi)$.

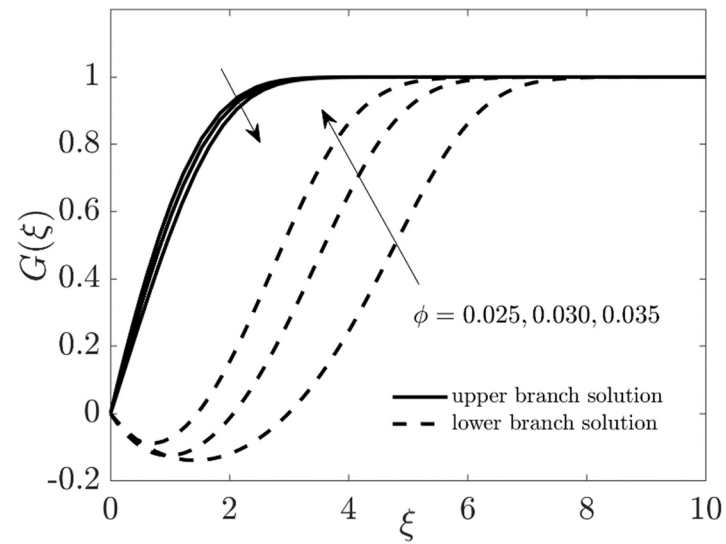


Figure 19. Impact of ϕ on $G(\xi)$.

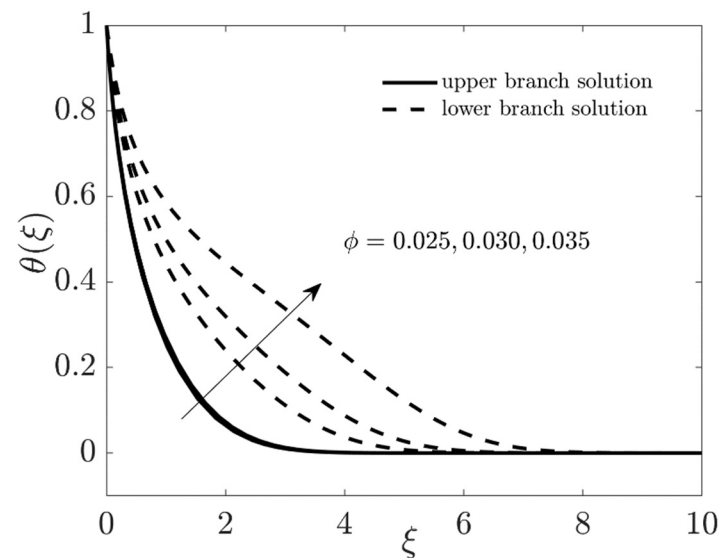


Figure 20. Impact of ϕ on $\theta(\xi)$.

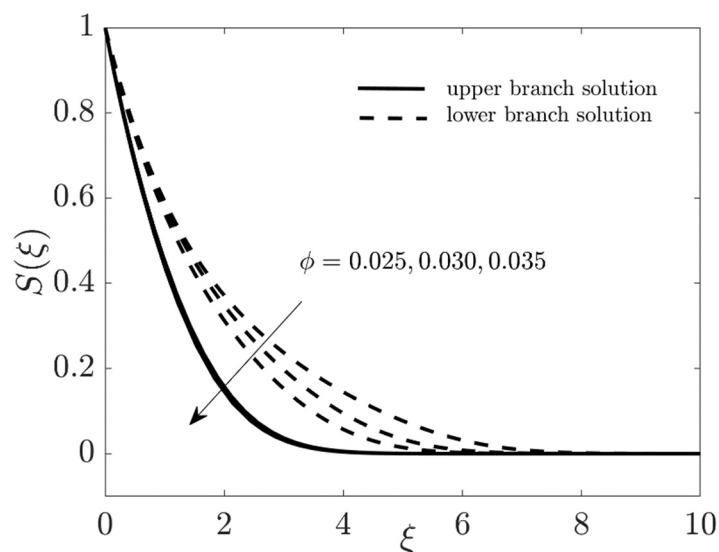


Figure 21. Impact of ϕ on $S(\xi)$.

Finally, Figure 22 illustrates the impacts of β_d on $S(\xi)$ for the upper and lower solution branches of the Al_2O_3 -water nanofluid. For increasing values of β_d , as a result, $S(\xi)$ shrinks in both dissimilar solution branches. More precisely, the concentration profiles and the thickness of the boundary layer are decelerated by improving the consequences of β_d . Physically, an enhancement in β_d leads to augments in the term $(1 + \delta_d\theta)^m \beta_d \exp[-e_d/1 + \delta_d\theta]$. As a result, the harmful chemical reaction that lowers the concentration profile is aided.

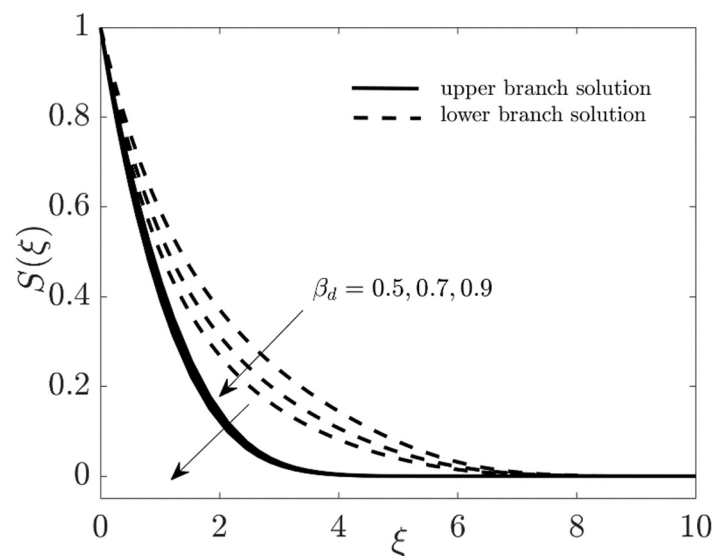


Figure 22. Impact of β_d on $S(\xi)$.

5. Conclusions

In this study, we used the Koo–Kleinstreuer and Li (KKL) model to study MHD three-dimensional nanofluid flow, as well as heat and mass transfer in the secondary-flow and streamwise directions. The inspirations of the binary chemical reaction and activation energy along with the effects of Soret and Dufour are also discussed. The similarity technique is employed to change our model from PDEs to ODEs, and then a numerical scheme bvp4c is used to solve the transmuted equations. The dual-nature outcomes are physically interpreted and discussed with the help of various graphs. The applicable scheme is also validated graphically with the available published work. The substantial points of the problem are summarized as:

- The concentration field shrinks in the stable and unstable solution branches due to the superior values of f_w , β_d , and ϕ . On the other hand, the temperature fields upsurge in both solution branches with increasing ϕ , while they are reduced due to f_w .
- The velocity fields in the x_h - and z_h -axes directions increase in the branch of the upper result and decrease in the branch of the lower result owing to the higher values of f_w , while the behavior of the velocity fields in x_h - and z_h -axes for both branches are reversed due to the larger values of ϕ .
- The heat transfer declines, but the mass transfer escalates in the upper branch, as well as in the lower branch, due to the increasing values of the Dufour number, while the trend or pattern of the outcomes appears completely reversed for the effects of the Soret number.
- The mass transfer rate increased in the upper branch solution due to the successive increment in the value of e_d and δ_d , while the behavior of the outcomes is altered in the lower branch solution.
- The friction factor upsurges in x_h - and z_h -axes for the upper branch solution due to the larger value of f_w , while it is reduced for the lower branch solution.

Author Contributions: Conceptualization, U.K., J.B., A.Z. and M.R.E.; methodology, U.K., F.S.A.-M., N.I. and M.R.E.; software, U.K. and M.R.E.; validation, U.K., J.B., A.Z., F.S.A.-M. and M.R.E.; formal analysis, U.K., A.Z., A.N.A. and M.R.E.; investigation, N.I., A.N.A. and M.R.E.; resources, U.K. and M.R.E.; data curation, A.Z., F.S.A.-M., N.I. and M.R.E.; writing—original draft preparation, U.K., A.Z., F.S.A.-M. and M.R.E.; writing—review and editing, U.K. and M.R.E.; visualization, U.K., A.Z., A.N.A. and M.R.E.; supervision, J.B. and A.N.A.; project administration, M.R.E.; funding acquisition, J.B. and A.N.A. All authors have read and agreed to the published version of the manuscript.

Funding: This research was funded by the Deanship of Scientific Research at Taif University, Taif, Saudi Arabia, Grant No. TURSP-2020/319.

Institutional Review Board Statement: Not Applicable.

Informed Consent Statement: Not Applicable.

Data Availability Statement: The results of this study are available only within the paper to support the data.

Acknowledgments: The authors express their appreciation to the Deanship of Scientific Research at Taif University, Taif, Saudi Arabia, for funding this work through the research groups program under Grant No. (TURSP-2020/319).

Conflicts of Interest: Concerning this manuscript, we have no conflicts of interest.

Nomenclature

x_h, y_h, z_h	Cartesian coordinates (m)
U_d	Uniform velocity (m/s)
B_h	Variable magnetic field (T)
B_0	Magnetic field Strength
u_h, v_h, w_h	Velocity components (m/s)
p_h	Pressure (Pa)
W_d	Constant ambient velocity (m/s)
T_h	Temperature (K)
C_h	Concentration
T_∞	Constant ambient temperature (K)
C_∞	Constant ambient concentration
v_d	Mass flux velocity (m/s)
D_m	Coefficient of mass diffusivity (m^2/s)
c_s	Concentration of susceptibility
k_T	Thermal diffusion ratio (m^2/s)
c_p	Specific heat at constant pressure (J/KgK)
T_m	Main fluid temperature (K)

D_B	Brownian diffusion coefficient
m	Rate of fitted constant
κ_d	Boltzmann constant
k_{rd}^2	Constant of chemical reaction rate
E_d	Activation energy
R_f	Thermal interfacial resistance (Km^3/W)
F, G	Dimensionless stream function
S	Concentration of nanoparticle
C_w	Constant wall surface concentration
T_w	Constant wall surface temperature (K)
M	Magnetic parameter
Du_d	Dufour number
Pr	Prandtl number
Le_d	Lewis number
Sr_d	Soret number
e_d	Activation parameter
f_w	Mass suction parameter
C_{Fx_h}, C_{Gz_h}	Coefficient of skin friction in x - and y -directions
k	Thermal conductivity
Nu_{x_h}	Local Nusselt number
Re_{x_h}	Local Reynolds number
Sh_{x_h}	Local Sherwood number
Greek symbols	
ε_d	Moving parameter (stretching/shrinking parameter)
ρ	Density
σ	Electrical conductivity
μ	Absolute viscosity
ν	Kinematic viscosity
ξ	similarity variable
ψ_d	Stream function
θ	Dimensionless temperature
δ_d	Temperature difference parameter
β_d	Reaction rate parameter
Acronyms	
KKL	Koo–Kleinstreuer and Li
3D	Three-dimensional
PDEs	Partial differential equations
ODEs	Ordinary differential equations
bvp4c	Boundary value problem of fourth-
orderBCR	Binary Chemical reaction
CBLF	Cross-boundary-layer flow
BL	Boundary layer
MHD	Magnetohydrodynamics
AAE	Arrhenius activation energy
TCN	Thermal conductivity
BMN	Brownian motion
Subscripts	
Al_2O_3	Aluminum dioxide nanoparticles
w	Condition at surface
nf	Nanofluid
∞	Ambient condition
f	Base fluid
f	Base fluid
Superscript	
$'$	Differentiation with respect to ξ

References

1. Jones, R.T. Effects of sweepback on boundary-layer and separation. *Rep. Nat. Adv. Comm. Aer.* **1947**, Washington No. 884. Available online: <https://digital.library.unt.edu/ark:/67531/metadc53671/> (accessed on 28 November 2021).
2. Mager, A. Three-dimensional laminar boundary layer with small cross-flow. *J. Aeronaut. Sci.* **1954**, *21*, 835–845. [[CrossRef](#)]
3. Dwyer, H.A. Solution of a three-dimensional boundary-layer flow with separation. *AIAA J.* **1968**, *6*, 1336–1342. [[CrossRef](#)]
4. Loos, H.G. A simple laminar boundary layer with secondary flow. *J. Aeronaut. Sci.* **1955**, *22*, 35–40. [[CrossRef](#)]
5. Na, T.Y.; Hansen, A.G. Similarity solutions of a class of laminar three-dimensional boundary layer equations of power law fluids. *Int. J. Non-Linear Mech.* **1967**, *2*, 373–385. [[CrossRef](#)]
6. Karabulut, H.; Ataer, Ö.E. Numerical solution of boundary layer equations in compressible cross-flow to a cylinder. *Int. J. Heat Mass Transf.* **1998**, *41*, 2677–2685. [[CrossRef](#)]
7. Fang, T.; Lee, C.-F.F. Three-dimensional wall-bounded laminar boundary layer with span-wise cross free stream and moving boundary. *Acta Mech.* **2008**, *204*, 235–248. [[CrossRef](#)]
8. Bhattacharyya, K.; Pop, I. Heat transfer for boundary layers with cross flow. *Chin. Phys. B* **2014**, *23*, 024701. [[CrossRef](#)]
9. Weidman, P. Similarity solutions for power-law and exponentially stretching plate motion with cross flow. *Int. J. Non-Linear Mech.* **2017**, *89*, 127–131. [[CrossRef](#)]
10. Weidman, P.D. New solutions for laminar boundary layers with cross flows driven by boundary motion. *Acta Mech.* **2017**, *228*, 1979–1991. [[CrossRef](#)]
11. Haq, R.-U.; Soomro, F.A.; Khan, Z.H.; Al-Mdallal, Q.M. Numerical study of streamwise and cross flow in the presence of heat and mass transfer. *Eur. Phys. J. Plus* **2017**, *132*, 214. [[CrossRef](#)]
12. Alfvén, H. Existence of electromagnetic-hydrodynamic waves. *Nature* **1942**, *150*, 405–406. [[CrossRef](#)]
13. Ali, F.M.; Nazar, R.; Arifin, N.M.; Pop, I. Dual solutions in MHD flow on a nonlinear porous shrinking sheet in a viscous fluid. *Bound. Value Probl.* **2013**, *2013*, 32. [[CrossRef](#)]
14. Salem, A. On the effectiveness of variable properties and thermophoresis on steady MHD heat and mass transfer over a porous flat surface. *Eng. Comput.* **2012**, *29*, 419–440. [[CrossRef](#)]
15. Aurangzaib; Bhattacharyya, K.; Shafie, S. Effect of partial slip on an unsteady MHD mixed convection stagnation-point flow of a micropolar fluid towards a permeable shrinking sheet. *Alex. Eng. J.* **2016**, *55*, 1285–1293. [[CrossRef](#)]
16. Azam, M.; Khan, M.; Alshomrani, A. Unsteady radiative stagnation point flow of MHD carreau nanofluid over expanding/contracting cylinder. *Int. J. Mech. Sci.* **2017**, *130*, 64–73. [[CrossRef](#)]
17. Sheikholeslami, M. Application of Darcy law for nanofluid flow in a porous cavity under the impact of Lorentz forces. *J. Mol. Liq.* **2018**, *266*, 495–503. [[CrossRef](#)]
18. Rabbi, K.M.; Sheikholeslami, M.; Karim, A.; Shafee, A.; Li, Z.; Tlili, I. Prediction of MHD flow and entropy generation by Artificial Neural Network in square cavity with heater-sink for nanomaterial. *Phys. A Stat. Mech. Its Appl.* **2020**, *541*, 123520. [[CrossRef](#)]
19. Ghadikolaei, S.; Gholinia, M. 3D mixed convection MHD flow of GO-MoS₂ hybrid nanoparticles in H₂O-(CH₂OH)₂ hybrid base fluid under the effect of H₂ bond. *Int. Commun. Heat Mass Transf.* **2020**, *110*, 104371. [[CrossRef](#)]
20. Abel, S.; Veena, P.; Rajgopal, K.; Pravin, V. Non-Newtonian magnetohydrodynamic flow over a stretching surface with heat and mass transfer. *Int. J. Non-Linear Mech.* **2004**, *39*, 1067–1078. [[CrossRef](#)]
21. Anilkumar, D.; Roy, S.J. Unsteady mixed convection flow on a rotating cone in a rotating fluid. *Appl. Math. Comput.* **2004**, *155*, 545–561. [[CrossRef](#)]
22. Chen, C.-H. Combined heat and mass transfer in MHD free convection from a vertical surface with Ohmic heating and viscous dissipation. *Int. J. Eng. Sci.* **2004**, *42*, 699–713. [[CrossRef](#)]
23. Parmar, H.; Timol, M.G. Deductive group technique for MHD coupled heat and mass transfer natural convection flow of non-Newtonian power law fluid over a vertical cone. *Int. J. Appl. Math Mech.* **2011**, *7*, 35–50.
24. Kandasamy, R.; Periasamy, K.; Prabhu, K.S. Chemical reaction, heat and mass transfer on MHD flow over a vertical stretching surface with heat source and thermal stratification effects. *Int. J. Heat Mass Transf.* **2005**, *48*, 4557–4561. [[CrossRef](#)]
25. Afify, A.A. MHD free convective flow and mass transfer over a stretching sheet with chemical reaction. *Heat Mass Transf.* **2004**, *40*, 495–500. [[CrossRef](#)]
26. Rahman, M.M.; Al-Lawatia, M. Effects of higher order chemical reaction on micropolar fluid flow on a power law permeable stretched sheet with variable concentration in a porous medium. *Can. J. Chem. Eng.* **2010**, *88*, 23–32. [[CrossRef](#)]
27. Bestman, A.R. Natural convection boundary layer with suction and mass transfer in a porous medium. *Int. J. Energy Res.* **1990**, *14*, 389–396. [[CrossRef](#)]
28. Mebine, P.; Gumus, R.H. On steady MHD thermally radiating and reacting thermosolutal viscous flow through a channel with porous medium. *Int. J. Math. Math. Sci.* **2010**, *2010*, 287435. [[CrossRef](#)]
29. Khan, M.I.; Hayat, T.; Alsaedi, A. Activation energy impact in nonlinear radiative stagnation point flow of Cross nanofluid. *Int. Commun. Heat Mass Transf.* **2018**, *91*, 216–224. [[CrossRef](#)]
30. Reddy, S.R.R.; Reddy, P.B.A.; Bhattacharyya, K. Effect of nonlinear thermal radiation on 3D magneto slip flow of Eyring-Powell nanofluid flow over a slendering sheet inspired through binarychemical reaction and Arrhenius activation energy. *Adv. Powder Tech.* **2019**, *30*, 3203–3213. [[CrossRef](#)]

31. Khan, U.; Zaib, A.; Khan, I.; Nisar, K.S. Activation energy on MHD flow of titanium alloy (Ti6Al4V) nanoparticle along with a cross flow and stream-wise direction with binary chemical reaction and non-linear radiation: Dual Solutions. *J. Material Res. Tech.* **2020**, *9*, 188–199. [[CrossRef](#)]
32. Mansour, M.; El-Anssary, N.; Aly, A. Effects of chemical reaction and thermal stratification on MHD free convective heat and mass transfer over a vertical stretching surface embedded in a porous media considering Soret and Dufour numbers. *Chem. Eng. J.* **2008**, *145*, 340–345. [[CrossRef](#)]
33. Prasad, V.R.; Vasu, B.; Bég, O.A. Thermo-diffusion and diffusion-thermo effects on MHD free convection flow past a vertical porous plate embedded in a non-Darcian porous medium. *Chem. Eng. J.* **2011**, *173*, 598–606. [[CrossRef](#)]
34. Pal, D.; Mondal, H. MHD non-Darcian mixed convection heat and mass transfer over a non-linear stretching sheet with Soret–Dufour effects and chemical reaction. *Int. Commun. Heat Mass Transf.* **2011**, *38*, 463–467. [[CrossRef](#)]
35. Zaib, A.; Shafie, S. Thermal diffusion and diffusion thermo effects on unsteady MHD free convection flow over a stretching surface considering Joule heating and viscous dissipation with thermal stratification, chemical reaction and Hall current. *J. Frankl. Inst.* **2014**, *351*, 1268–1287. [[CrossRef](#)]
36. Reddy, P.S.; Chamkha, A.J. Soret and Dufour effects on MHD convective flow of Al₂O₃–water and TiO₂–water nanofluids past a stretching sheet in porous media with heat generation/absorption. *Adv. Powder Technol.* **2016**, *27*, 1207–1218. [[CrossRef](#)]
37. Khan, M.I.; Waqas, M.; Hayat, T.; Alsaedi, A. Soret and Dufour effects in stretching flow of Jeffrey fluid subject to Newtonian heat and mass conditions. *Results Phys.* **2017**, *7*, 4183–4188. [[CrossRef](#)]
38. Idowu, A.S.; Falodun, B.O. Soret–Dufour effects on MHD heat and mass transfer of Walter’s-B viscoelastic fluid over a semi-infinite vertical plate: Spectral relaxation analysis. *J. Taibah Univ. Sci.* **2018**, *13*, 49–62. [[CrossRef](#)]
39. Devi, S.S.U.; Devi, S.A. Numerical investigation of hydromagnetic hybrid Cu–Al₂O₃/ water nanofluid flow over a permeable stretching sheet with suction. *Int. J. Nonlinear Sci. Numer. Simul.* **2016**, *17*, 249–257. [[CrossRef](#)]
40. Soid, S.K.; Ishak, A.; Pop, I. Boundary layer flow past a continuously moving thin needle in a nanofluid. *Appl. Therm. Eng.* **2017**, *114*, 58–64. [[CrossRef](#)]
41. Aly, E.; Pop, I. MHD flow and heat transfer over a permeable stretching/shrinking sheet in a hybrid nanofluid with a convective boundary condition. *Int. J. Numer. Methods Heat Fluid Flow* **2019**, *29*, 3012–3038. [[CrossRef](#)]
42. Islami, S.B.; Dastvareh, B.; Gharraei, R. An investigation on the hydrodynamic and heat transfer of nanofluid flow, with non-Newtonian base fluid, in micromixers. *Int. J. Heat Mass Transf.* **2014**, *78*, 917–929. [[CrossRef](#)]
43. Elgazery, N.S. Flow of non-Newtonian magneto-fluid with gold and alumina nanoparticles through a non-Darcian porous medium. *J. Egypt. Math. Soc.* **2019**, *27*, 39. [[CrossRef](#)]
44. Hakeem, A.K.A.; Kirusakthika, S.; Ganga, B.; Khan, M.I.; Nayak, M.K.; Muhammad, T.; Khan, S.U. Transverse magnetic effects of hybrid nanofluid flow over a vertical rotating cone with Newtonian/non-Newtonian base fluids. *Waves Random Complex Media* **2021**, 1–18. [[CrossRef](#)]
45. Kandelousi, M.S. KKL correlation for simulation of nanofluid flow and heat transfer in a permeable channel. *Phys. Lett. A* **2014**, *378*, 3331–3339. [[CrossRef](#)]
46. Haq, R.U.; Usman, M.; Algehyne, E.A. Natural convection of CuO–water nanofluid filled in a partially heated corrugated cavity: KKL model approach. *Commun. Theor. Phys.* **2020**, *72*, 085003. [[CrossRef](#)]
47. Alsagri, A.S.; Moradi, R. Application of KKL model in studying of nanofluid heat transfer between two rotary tubes. *Case Stud. Therm. Eng.* **2019**, *14*, 100478. [[CrossRef](#)]
48. Sheikholeslami, M.; Mahian, O. Enhancement of PCM solidification using inorganic nanoparticles and an external magnetic field with application in energy storage systems. *J. Clean. Prod.* **2019**, *215*, 963–977. [[CrossRef](#)]
49. Nisar, K.S.; Khan, U.; Zaib, A.; Khan, I.; Baleanu, D. Exploration of aluminum and titanium alloys in the stream-wise and secondary flow directions comprising the significant impacts of magnetohydrodynamic and hybrid nanofluid. *Crystals* **2020**, *10*, 679. [[CrossRef](#)]
50. Zaib, A.; Haq, R.; Sheikholeslami, M.; Khan, U. Numerical analysis of effective Prandtl model on mixed convection flow of γ Al₂O₃–H₂O nanoliquids with micropolar liquid driven through wedge. *Phys. Scr.* **2019**, *95*, 035005. [[CrossRef](#)]
51. Alghamdi, M.; Wakif, A.; Thumma, T.; Khan, U.; Baleanu, D.; Rasool, G. Significance of variability in magnetic field strength and heat source on the radiative-convective motion of sodium alginate-based nanofluid within a Darcy-Brinkman porous structure bounded vertically by an irregular slender surface. *Case Stud. Therm. Eng.* **2021**, *28*, 101428. [[CrossRef](#)]
52. Koo, J.; Kleinstreuer, C. Viscous dissipation effects in microtubes and microchannels. *Int. J. Heat Mass Transf.* **2004**, *47*, 3159–3169. [[CrossRef](#)]
53. Koo, J. Computational Nanofluid Flow and Heat Transfer Analyses Applied to Micro-Systems. Ph.D. Thesis, NC State University, Raleigh, NC, USA, 2005.
54. Jang, S.P.; Choi, S.U.S. Role of Brownian motion in the enhanced thermal conductivity of nanofluids. *Appl. Phys. Lett.* **2004**, *84*, 4316–4318. [[CrossRef](#)]
55. Prasher, R.; Bhattacharya, P.; Phelan, P.E. Thermal conductivity of nanoscale colloidal solutions (nanofluids). *Phys. Rev. Lett.* **2005**, *94*, 025901. [[CrossRef](#)] [[PubMed](#)]

-
56. Li, J. Computational Analysis of Nanofluid Flow in Microchannels with Applications to Micro-Heat Sinks and Bio-MEMS. Ph.D. Thesis, NC State University, Raleigh, NC, USA, 2008.
 57. Dzulkifli, N.F.; Bachok, N.; Pop, I.; Yacob, N.A.M.; Arifin, N.M.; Rosali, H. Stability of partial slip, Soret and Dufour effects on unsteady boundary layer flow and heat transfer in Copper-water nanofluid over a stretching/shrinking sheet. *J. Phys. Conf. Ser.* **2017**, *890*, 12031. [[CrossRef](#)]